

Demonstrating Dynamic Stability in Paul Traps: Exploring Rotating Saddles with Liquid Nitrogen Droplets

Laurel Barnett,^{*} Aidan Carey,[†] Robert Hart,[‡] Daniel Davis,[§] Anna Klales,[¶] and Louis Deslauriers^{**}
Department of Physics, Harvard University, Cambridge, MA 02138

(Dated: May 8, 2025)

Rotating saddle potentials provide a compelling visual demonstration of dynamic stability, widely used in undergraduate physics as mechanical analogs to the RF Paul trap. Traditional demonstrations typically rely on rolling ball bearings, whose frictional effects and internal rotation obscure fundamental particle dynamics. We introduce a simple yet significant improvement by employing droplets of liquid nitrogen (LN_2), which levitate via the Leidenfrost effect, eliminating rolling dynamics and greatly reducing friction. LN_2 droplets clearly illustrate the rotating ponderomotive-like force, producing trajectories closely consistent with theoretical predictions. Using experimental data, we compare the stability threshold and particle trajectories of LN_2 droplets and traditional ball bearings. LN_2 droplets exhibit a sharply defined and visually distinct stability threshold, transitioning abruptly from unstable to stable motion at a critical rotation frequency. In contrast, ball bearings demonstrate a more gradual threshold, accompanied by trajectories complicated by friction-induced deviations. We present detailed measurements of particle lifetimes and trajectories as functions of dimensionless stability parameters for both symmetric and intentionally asymmetric saddles. These improvements significantly enhance visual and conceptual clarity, reduce common misconceptions related to frictional dynamics, and provide natural opportunities for exploring related phenomena such as the Leidenfrost effect. We also offer practical guidance on assembling and implementing this enhanced demonstration for effective classroom and laboratory instruction.

I. INTRODUCTION

A saddle-shaped surface rotating about its inflection point can dynamically stabilize and confine a particle near its center, a visually compelling demonstration frequently used in undergraduate physics education. This stabilization occurs when the angular velocity of rotation surpasses a critical threshold, converting an otherwise unstable equilibrium into a dynamically stable one [1, 2]. Rotating saddle demonstrations vividly illustrate dynamic stability, a fundamental phenomenon central to many physical systems, including RF Paul traps, Rydberg atoms confined by rotating electric fields, Lagrange points of celestial mechanics, and recently identified gravitational saddle potentials near charged binary black hole systems [3–11]. These examples underscore the broad relevance of rotating saddle dynamics across classical, quantum, and astrophysical contexts.

Typical classroom implementations use spherical objects — often steel ball bearings — whose rolling friction and internal rotation cause their motion to differ significantly from the idealized dynamics of a point particle trapped in a rotating saddle [12–15]. In practice, observers readily notice these complications: rolling balls often exhibit erratic, swirling trajectories that clearly reflect significant frictional interaction with the rotating saddle. These frictional effects make it difficult to observe cleanly the characteristic dynamics expected from a rotating potential. Moreover, successful demonstrations typically require carefully dropping the ball nearly at rest

and precisely at the saddle’s center to maximize trapping lifetimes, a challenging task that further limits the effectiveness of the demonstration.

We introduce a straightforward yet highly effective improvement: replacing rolling spheres with droplets of liquid nitrogen (LN_2). Due to the Leidenfrost effect, these droplets levitate on a thin vapor cushion formed by rapid evaporation, eliminating rolling dynamics and greatly reducing friction [16, 17]. Consequently, their motion closely approximates frictionless particle dynamics, substantially enhancing pedagogical clarity.

The primary advantage of LN_2 droplets is that their motion clearly reveals the rotating nature of the confining force, producing trajectories consistent with theoretical predictions of a rotating saddle potential. In contrast, rolling balls exhibit trajectories visibly distorted by frictional coupling to the saddle surface, substantially diminishing the instructional clarity of the demonstration. Furthermore, the low-friction LN_2 droplets are relatively insensitive to initial positioning and velocity. Unlike rolling balls, LN_2 droplets do not require precise placement near the saddle center or careful initial velocity control. As we discuss in this paper, LN_2 droplets typically exhibit stable trapping even when initially deposited off-center or in motion.

An additional key benefit is the sharp transition between stability and instability exhibited by LN_2 droplets as the rotation frequency crosses the stability threshold. Even minute frequency adjustments produce a distinct, visual shift from stable trapping to rapid escape, making this demonstration particularly effective in highlighting the concept of dynamic stability thresholds.

Real-world analogs to rotating saddle traps, such as RF Paul traps used for precision quantum manipulation, often incorporate slight potential asymmetries to lift degeneracies in particle motion, facilitating laser cooling and quantum control

^{*} lj Barnett@college.harvard.edu

[†] aidanbcarey@gmail.com

[‡] roberthart56@gmail.com

[§] ddavis@fas.harvard.edu

[¶] aklales@g.harvard.edu

^{**} louis@physics.harvard.edu

[9, 18–20]. Motivated by this practical relevance, our demonstrations include saddles with both intentional asymmetry and symmetric geometry, allowing clear investigation into how subtle variations in symmetry affect particle trajectories and trapping stability [21].

In this paper, we describe the theoretical background, experimental implementation, and practical classroom use of the LN_2 rotating saddle demonstration. We quantify the substantial improvement in visual and quantitative fidelity compared to traditional rolling spheres by mapping the lifetime of LN_2 droplets as a function of the stability parameters a and q , which we vary experimentally by adjusting the rotation frequency [21]. We present lifetime data illustrating sharp threshold behavior, representative particle trajectories, and practical details about fabricating the saddles, assembling the demonstration apparatus, and effectively performing this compelling demonstration in educational settings. Beyond enhancing the understanding of dynamic stability and rotating saddle potentials, this demonstration also naturally introduces opportunities to explore related phenomena such as the Leidenfrost effect itself.

II. BACKGROUND THEORY

The motion of a particle on a rotating saddle surface can be described by considering the gravitational potential in a rotating reference frame. Following the derivation presented in detail by Carey et al. [21], we summarize the key equations and parameters relevant to understanding dynamic stability in our demonstration.

In the rotating frame, the gravitational potential for a saddle-shaped surface can be approximated by the hyperbolic form:

$$U(x', y') = \frac{mgh_0}{r_0^2} (\beta x'^2 - y'^2), \quad (1)$$

where m is the mass of the particle, g is gravitational acceleration, h_0 and r_0 represent geometric parameters of the saddle (the saddle height and radius, respectively), and β characterizes the curvature asymmetry of the saddle. A symmetric saddle corresponds to $\beta = 1$.

Transforming into the laboratory frame rotating with angular frequency Ω , and introducing the dimensionless time $\tau = \Omega t$, the equations of motion take the standard Mathieu-like form [12, 21]:

$$\frac{d^2x}{d\tau^2} + (a + 2q \cos(2\tau))x + 2q \sin(2\tau)y = 0, \quad (2)$$

$$\frac{d^2y}{d\tau^2} + (a - 2q \cos(2\tau))y + 2q \sin(2\tau)x = 0, \quad (3)$$

where the dimensionless parameters a and q are given by:

$$a = \frac{gh_0(\beta - 1)}{r_0^2\Omega^2}, \quad q = \frac{gh_0(\beta + 1)}{r_0^2\Omega^2}. \quad (4)$$

These parameters determine the stability of particle trajectories, analogous to the stability regions found in RF Paul

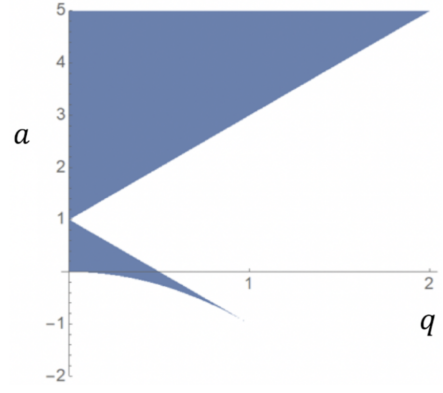


FIG. 1. Stability diagram for the rotating saddle potential, showing regions in the (a, q) parameter space where particle motion is stable (shaded blue). The stability boundary is analytically determined and forms a simple triangular region for positive a , with a sharp instability at $a = 1$. For negative a , stability terminates at $q = 1$, $a = -1$.

traps [22, 23]. Stability occurs when particle oscillations remain bounded within the saddle’s confines; instability corresponds to rapidly diverging trajectories. Carey et al. [21] provide detailed derivations and stability diagrams illustrating how stability conditions depend on these parameters.

Previous experimental implementations have typically employed spherical objects — such as steel balls or plastic spheres — as analog particles. However, rolling motion introduces frictional forces and internal rotation that lead to significant deviations from the idealized point-mass dynamics assumed in theoretical models. Notably, Kirillov and Levi [13] showed that rolling friction induces a precession analogous to that observed in a Foucault pendulum, while Fan et al. [14] demonstrated that certain deviations persist even as the ball radius tends to zero, indicating that the breakdown in correspondence with ideal trajectories is not merely a finite-size effect. These non-ideal behaviors obscure the essential features of dynamic stability and motivate the use of friction-minimizing alternatives.

In our experiments, we use liquid nitrogen (LN_2) droplets, which levitate via the Leidenfrost effect and closely approximate frictionless point-particle motion. Varying the saddle’s rotation frequency Ω tunes the dimensionless parameters a and q , allowing us to systematically explore the transition between stable and unstable regimes. The equations presented above provide a quantitative framework for interpreting the measured particle lifetimes and trajectories described in the following sections.

III. EXPERIMENTAL SETUP

The core of the demonstration consists of a 3D-printed saddle mounted on a motor via a custom 3D-printed adapter, as shown in Fig. 2.

The saddle is rotated by a stepper motor controlled by a microstep driver, which receives a frequency signal from a function generator. The driver is powered by an external voltage source. The output frequency of the function generator is

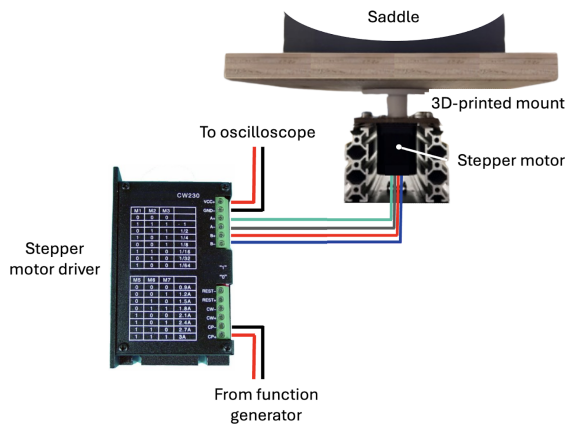


FIG. 2. Schematic of the rotating saddle demonstration setup, showing the motor, driver, function generator, and 3D-printed saddle mount.

monitored via a BNC connection to an oscilloscope, allowing precise control and real-time feedback on the rotation speed.

IV. DEMONSTRATION PROCEDURE

For large lecture settings, the demonstration is best projected using an overhead camera with a frame rate of at least 60 frames per second. When using LN_2 droplets, additional lighting (e.g., a directional lamp angled from above) can greatly enhance visibility. Further practical considerations are described below.

In our demonstrations, we use two 3D-printed saddles with different asymmetry coefficients: a nearly symmetric saddle with $\beta = 1.06$, and an asymmetric saddle with $\beta = 2.67$. Both saddles share identical geometric dimensions, characterized by a saddle height $h_0 = 2.5$ cm and a radius $r_0 = 9$ cm. These parameters define the saddle curvature and directly influence the particle dynamics. The nearly symmetric saddle ($\beta = 1.06$) corresponds to a vertical deviation of approximately 1.5 mm at the saddle's edge ($r_0 = 9$ cm) compared to a perfectly symmetric saddle ($\beta = 1.06$). Comparing these two saddles illustrates how small differences in geometry significantly affect the sharpness of the dynamic stability threshold and resulting particle trajectories. Unless otherwise stated, rotation frequencies and specific threshold behaviors described in this section refer to the asymmetric saddle ($\beta = 2.67$).

A. Trapping liquid nitrogen droplets

Each LN_2 bead is only a few millimeters in diameter, so for classroom visibility, the camera and lighting setup described above is particularly important.

Begin the demonstration by presenting students with a stationary saddle. Optionally, instructors may first display a photograph or CAD rendering of the saddle's profile to illustrate its geometry. Dispense a small quantity of LN_2 at the center of the saddle; students will immediately observe the liq-

uid nitrogen sliding down the negative curvature of the saddle. Fig. 3 provides a visual example of how LN_2 droplets evolve on the rotating saddle after dispensation; further details on optimal dispensing procedures and considerations are discussed later in this section. Before proceeding, instructors can engage students by prompting them to predict factors that might enable the LN_2 bead to remain trapped near the saddle's center once rotation begins. This approach aligns with research-based best practices for interactive demonstrations, which emphasize prediction, discussion, and conceptual reasoning to enhance student understanding [24, 25].

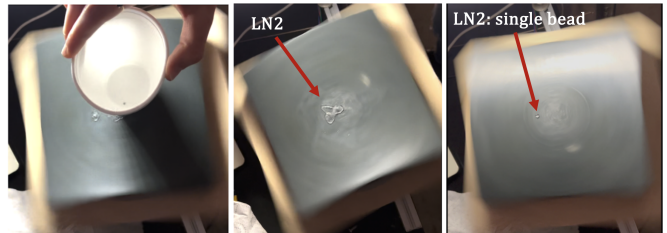


FIG. 3. Evolution of liquid nitrogen droplets on a rotating saddle over time.

Next, turn on the stepper motor at a rotational frequency below the expected stability threshold. For the saddle with positive asymmetry ($\beta = 2.67$), start at or below approximately 1.15 rotations per second (rps). After student predictions, dispense LN_2 onto the rotating saddle multiple times to clearly demonstrate instability—each bead will rapidly slide off the saddle surface.

After students recognize the instability, increase the rotation frequency incrementally, by approximately 50 millihertz (for instance, from 1.15 to 1.2 rps for the asymmetric saddle). Highlight to students that this extremely small change in rotation frequency, barely noticeable by the naked eye, dramatically alters the system's behavior. Repeat the dispensation of LN_2 at the increased frequency. With the asymmetric saddle at 1.2 rps, typical trapping times increase dramatically, shifting from nearly immediate ejection to average lifetimes exceeding 15 seconds. Small differences in initial placement or velocity do not significantly affect trapping success, illustrating the robustness and sensitivity of the system at this threshold. This sharp threshold behavior is clearly illustrated in Fig. 4, which shows measured trapping times of LN_2 droplets as a function of rotation frequency.

A final trial at a higher frequency (approximately 1.5 rps for the asymmetric saddle) demonstrates even more pronounced stability, often yielding trapping times exceeding 30 seconds. For the nearly symmetric saddle ($\beta = 1.06$), the stability region will be shifted slightly but still observable. Instructors should perform similar incremental trials, emphasizing how subtle differences in saddle geometry affect the stability threshold.

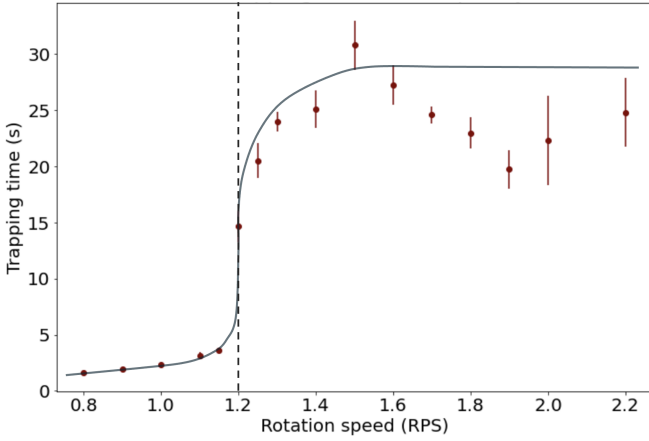


FIG. 4. Measured lifetime of LN_2 bead in rotating saddle as a function of rotation frequency in rps, showing the sharp threshold at $\Omega \approx 1.2$ rps.

B. Mapping stability with dimensionless parameters

To visualize the dependence of particle stability on rotation frequency and saddle geometry, we plot the measured lifetimes for LN_2 droplets as a function of the dimensionless stability parameters a and q in a composite stability diagram, shown in Fig. 5. This figure shows data from both the nearly symmetric ($\beta = 1.06$) and asymmetric ($\beta = 2.67$) saddles, allowing direct comparison of their stability boundaries and threshold sharpness. Each data point represents an experimental trial at a given rotation frequency Ω , translated into a and q using Eq. (4).

The grayscale intensity of each data point indicates the normalized trapping lifetime: completely white corresponds to the longest recorded lifetime (normalized to 1.0), while completely black indicates immediate bead ejection (zero normalized lifetime). Intermediate shades represent proportionally shorter lifetimes. Thus, this plot visually highlights the sharp threshold behavior characteristic of rotating saddle stability, where even small changes in rotational frequency (and thus small changes in a and q) can lead to dramatic differences in particle confinement times. The asymmetric saddle ($\beta = 2.67$) data points near the stability threshold correspond exactly to the sharp transition in trapping lifetime previously illustrated in Fig. 5, but are now plotted explicitly in terms of the dimensionless stability parameters a and q . In contrast, as we will show later, ball bearings exhibit a notably more gradual and less distinct threshold in the a - q stability space.

For a given saddle geometry (defined by β , h_0 , and r_0), varying the rotation frequency Ω traces out a straight line in the a - q stability space, described by:

$$a = 2 \frac{\beta - 1}{\beta + 1} q. \quad (5)$$

This explains why experimental points for each saddle in Fig. 5 lie along distinct linear trajectories.

1. Dispensing liquid nitrogen onto the saddle

Pipettes and other traditional dispensers often become clogged with condensation, making them unreliable for delivering LN_2 to a rotating saddle. The most consistent method we found involved an 8-ounce styrofoam cup with a small (approximately 2 mm-wide) hole punched near the lower rim. Holding the cup above the center of the saddle and gently tipping it allows for controlled pouring through the punched hole.

To maximize observable trapping time, the initial pool of LN_2 on the saddle should be roughly the size of a quarter. In stable conditions, most of the liquid near the edges quickly runs off, leaving a few smaller, self-forming droplets near the center. We define the “lifetime” of a dispensation as the duration between the initial pour and the final bead’s departure from the saddle. Fig. 3 shows the evolution of LN_2 droplets after dispensation.

After several trials—or after a particularly long-lived run—condensation may accumulate at the saddle’s center. If this occurs, the saddle should be warmed using a hair dryer or heat gun, and any remaining water wiped away. This step is essential to prevent immediate boiling and to maintain the Leidenfrost effect for subsequent trials.

V. COMPARATIVE RESULTS: LN_2 vs. BALL BEARINGS

While rotating saddles traditionally employ rolling objects such as ball bearings to illustrate dynamic stability, we have demonstrated significant pedagogical advantages in using droplets of liquid nitrogen (LN_2). Below we explicitly compare these two approaches, emphasizing differences in fidelity to theoretical predictions, clarity of visual demonstrations, and overall instructional impact.

A. Stability threshold and lifetime comparisons

As previously demonstrated, the LN_2 bead exhibits a sharply defined stability threshold around a rotation frequency of approximately 1.2 rps (Fig. 4). This precise threshold results from the minimal friction and negligible internal rotation associated with Leidenfrost levitation, closely matching theoretical predictions for a frictionless particle.

In contrast, ball bearings exhibit a more gradual transition to stability, occurring at slightly higher rotational frequencies (approximately 1.25–1.3 rps in our setup). This less distinct threshold results from frictional effects and internal rolling motion, causing trajectories to deviate notably from theoretical predictions [12, 14]. Fig. 6 explicitly illustrates these differences by plotting measured trapping lifetimes for ball bearings as a function of the dimensionless stability parameters a and q for both asymmetric ($\beta = 2.67$) and nearly symmetric ($\beta = 1.06$) saddles. Unlike the sharp, clearly defined threshold observed with LN_2 droplets (Fig. 4 and Fig. 5), ball bearings display a broader stability region and a less distinct boundary. Additionally, the segment of stable trapping (darkest data points) is notably shorter compared to LN_2 droplets,

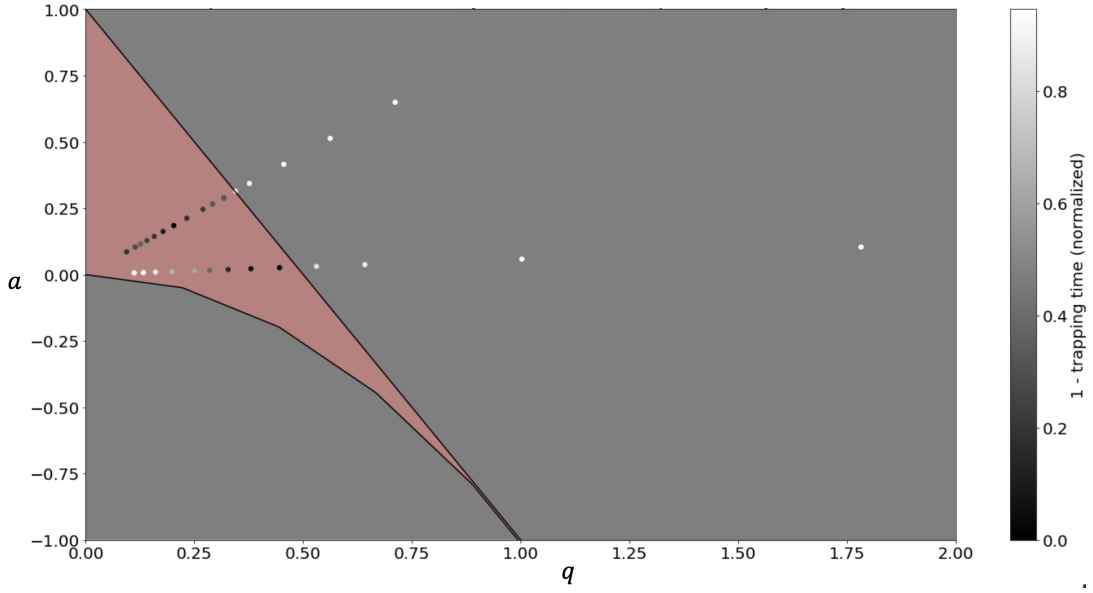


FIG. 5. Measured stability regions for LN₂ droplets in rotating saddles with asymmetry parameters $\beta = 2.67$ (asymmetric) and $\beta = 1.06$ (nearly symmetric), plotted on the a - q stability diagram. The grayscale indicates normalized lifetime, where darker points represent longer lifetimes.

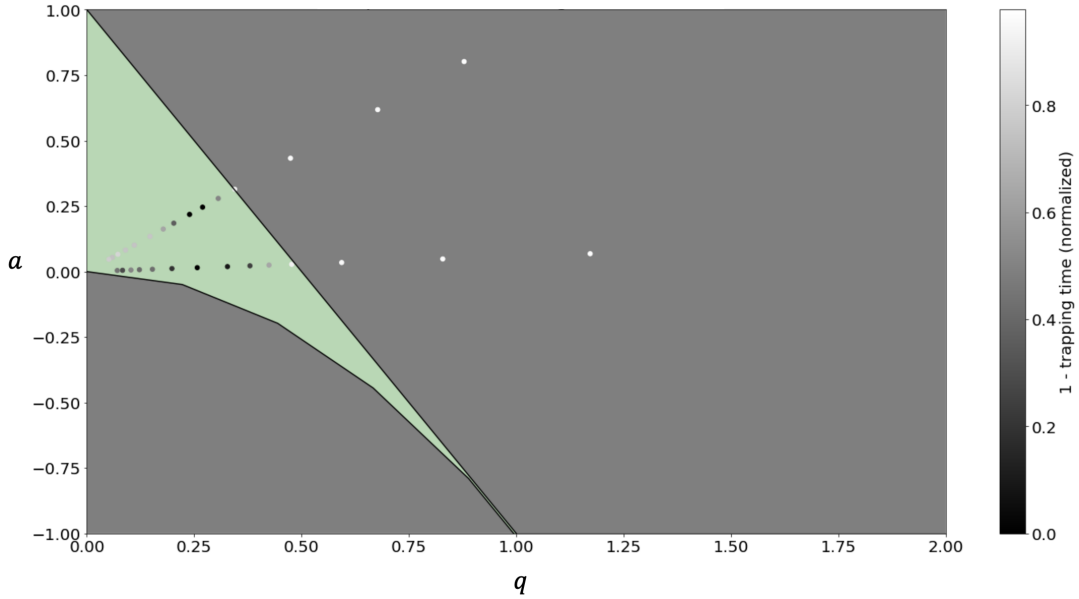


FIG. 6. Measured stability regions for ball bearings in rotating saddles with asymmetry parameters $\beta = 2.67$ (asymmetric) and $\beta = 1.06$ (nearly symmetric), plotted on the a - q stability diagram. The grayscale indicates normalized lifetime, with darker points representing longer lifetimes.

further highlighting the diminished instructional clarity inherent to demonstrations relying on rolling objects.

B. Particle trajectory comparisons

Figures 7 and 8 directly illustrate the fundamental differences in particle dynamics between ball bearings and LN₂

droplets. Fig. 7 shows the observed trajectory of a ball bearing (left), characterized by an exponential outward spiral with smoothed features resulting from friction and rolling effects. To an observer, these trajectories appear visibly dominated by surface interaction rather than by the expected potential dynamics. These non-ideal effects clearly suppress the intricate trajectory structure predicted for an ideal frictionless particle (right), reducing both visual clarity and conceptual coherence.

In sharp contrast, Fig. 8 displays the trajectory of an LN_2 droplet (left), which more closely resembles the theoretical prediction (right). The Leidenfrost levitation significantly reduces friction, allowing trajectories that visibly retain the intricate, rotating ponderomotive-like features predicted by theory. An observer can readily discern the complex orbital patterns expected from the theoretical model, making the underlying physics immediately apparent. Consequently, its trajectory clearly illustrates the rotating saddle's confining force, substantially enhancing the demonstration's visual and conceptual impact.

These visual comparisons highlight the pedagogical advantage of LN_2 droplets over traditional ball bearings, emphasizing their enhanced fidelity to theoretical dynamics and greater effectiveness as instructional tools.

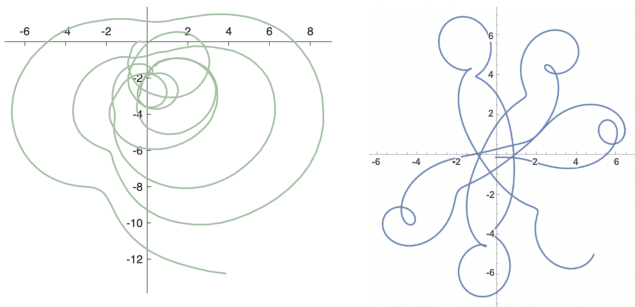


FIG. 7. A comparison of the observed trajectory of a ball bearing (left) vs. the predicted trajectory of an ideal particle (right) in a saddle with asymmetry parameter $\beta = 1.06$ and rotational frequency $\Omega = 1.2$ over a period of 8.91 seconds. Initial conditions: $(x_0, y_0, v_{x0}, v_{y0}) = (-0.052 \text{ cm}, -0.125 \text{ cm}, 0.152 \text{ cm/s}, -0.125 \text{ cm/s})$. The observed trajectory spirals outward exponentially, exhibiting a smoothed trajectory due to friction and rolling effects.

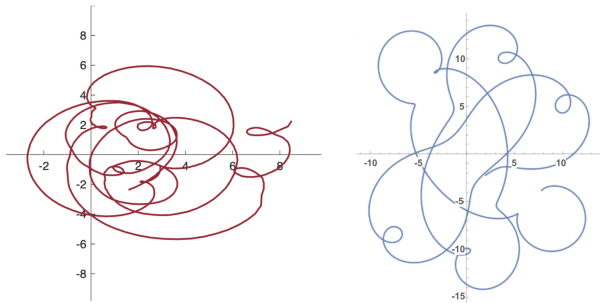


FIG. 8. A comparison of the observed trajectory of LN_2 (left) vs. the predicted trajectory of an ideal particle (right) in a saddle with asymmetry parameter $\beta = 1.06$ and rotational frequency $\Omega = 1.2$ over a period of 9.28 seconds. Initial conditions: $(x_0, y_0, v_{x0}, v_{y0}) = (1.953 \text{ cm}, -2.171 \text{ cm}, 1.646 \text{ cm/s}, 2.405 \text{ cm/s})$. The observed trajectory more closely resembles theoretical predictions, clearly illustrating the rotating ponderomotive-like nature of the confining force.

VI. APPLICATIONS AND EDUCATIONAL VALUE

Quadrupole ion traps (RF Paul traps) have broad relevance in modern physics, underpinning essential technologies such as atomic clocks and quantum computing. Incorporating the rotating saddle demonstration into undergraduate courses—such as classical mechanics, electromagnetism, or introductory quantum mechanics—provides tangible, real-world context to otherwise abstract theoretical principles.

Moreover, this demonstration offers an engaging platform for active student participation, prediction, and discussion. Given its simplicity, clarity, and direct analogy to modern experimental systems, it can be effectively adapted into interactive lecture demonstrations, group laboratory exercises, or student-driven final projects.

VII. CONCLUSION

We have demonstrated significant improvements over the traditional rotating saddle demonstration of dynamic stability by employing liquid nitrogen (LN_2) droplets levitating via the Leidenfrost effect. Unlike standard rolling ball bearings, LN_2 droplets minimize friction and internal rotation, more accurately approximating the theoretical dynamics of an ideal, frictionless particle. Furthermore, subtle saddle asymmetries provide additional realism, closely modeling potentials encountered in actual RF Paul traps.

These modifications lead to a clearer, more accurate, and more pedagogically relevant demonstration. Specifically, LN_2 droplets exhibit a sharper and more distinct stability threshold compared to traditional ball bearings, effectively eliminating common misconceptions caused by frictional and rolling dynamics. We recommend this improved demonstration for clearly illustrating dynamic stability principles in undergraduate physics instruction.

ACKNOWLEDGMENTS

We are grateful for helpful discussions with Gregory Kestin and Logan McCarty. We gratefully acknowledge support from the Faculty of Arts and Sciences at Harvard University. GPT-4 [26] was used to refine this manuscript.

AUTHOR DECLARATIONS

The authors have no conflicts to disclose.

APPENDIX

A. Saddle fabrication

Saddles of varying asymmetry were designed using .stl files generated by a Python script (Appendix: Python script for saddle geometry). Saddles were printed using PETG filament on a Prusa Original i3 printer. Models were scaled to 173% of their original size for an 18 cm square base, printed with 30% infill for durability. Dark filament colors improved visibility. Print times ranged from 33 to 52 hours, consuming roughly

two-thirds of a kilogram per saddle.

Once printed and cooled, saddles were sanded with an electric sander, followed by hand-sanding with fine-grit sandpaper. Care was taken to preserve the intended curvature. Saddles were then coated with Smooth-On XTC-3D under a fume hood, curing overnight. Minor surface imperfections post-curing were gently sanded by hand.

Optionally, saddles were mounted to wooden boards slightly larger than the saddle bases to address any minor deformations. A central hole drilled into the saddle base and board allowed alignment with a dowel, centering the saddle. Hot glue secured the saddle to the board, correcting slight deformations.

A cylindrical motor mount was 3D-printed separately using PLA filament. The mount included openings for the motor axle and centering dowel. Four self-tapping screws attached the mount to the board, with a horizontal screw securing the motor axle.

B. Setup Assembly

The saddle was rotated using a StepperOnline Nema 17 Bipolar 2A stepper motor controlled by a StepperOnline CNC Motor Driver. A DC power supply providing at least 14.5V

was connected to the motor driver. The stepper motor was configured to 3200 steps per full rotation, with frequency controlled by a function generator (frequency monitored via an oscilloscope if necessary).

To minimize friction and improve rotation accuracy, the assembled saddle was elevated using a plywood rectangle attached to the motor. This plywood was secured with screws and wing-nuts to metal rails clamped to the demonstration table.

C. Materials and cost

The table below summarizes the primary components required for the rotating saddle demonstration, including vendors, estimated costs, and relevant comments. Although the table may appear later due to float placement, it is part of this subsection.

D. Python script for saddle geometry

A Python script used to generate .stl files for the saddle geometry is included at the end of the document. Users can modify the script to explore different asymmetries and curvatures.

-
- [1] W. Paul, Electromagnetic traps for charged and neutral particles, *Reviews of Modern Physics* **62**, 531 (1990).
 - [2] W. Rueckner *et al.*, Rotating saddle paul trap, *American Journal of Physics* **63**, 186 (1995).
 - [3] P. L. Kapitza, Dynamic stability of a pendulum when its point of suspension vibrates, *Soviet Physics JETP* **21**, 588–598 (1951).
 - [4] R. R. Whymark, Acoustic levitation of liquid drops, *Nature* **254**, 585–586 (1975).
 - [5] E. L. Raab, M. Prentiss, A. Cable, S. Chu, and D. E. Pritchard, Trapping of neutral sodium atoms with radiation pressure, *Physical Review Letters* **59**, 2631–2634 (1987).
 - [6] I. Bialynicki-Birula, M. Kalinski, and J. H. Eberly, Lagrange Equilibrium Points in Celestial Mechanics and Nonspreading Wave Packets for Strongly Driven Rydberg Electrons, *Physical Review Letters* **73**, 1777 (1994).
 - [7] C. D. Murray and S. F. Dermott, *Solar System Dynamics* (Cambridge University Press, 1999).
 - [8] H. G. Dehmelt, Radiofrequency spectroscopy of stored ions i: Storage, *Advances in Atomic and Molecular Physics* **3**, 53 (1967).
 - [9] D. Leibfried, R. Blatt, C. Monroe, and D. Wineland, Quantum dynamics of single trapped ions, *Reviews of Modern Physics* **75**, 281 (2003).
 - [10] K. Abe and T. Hasegawa, Quantum mechanics in rotating-radio-frequency traps and penning traps with a quadrupole rotating field, *Physical Review A* **81**, 033402 (2010).
 - [11] A. Kurmus, M. Zajacek, G. Kestin, and L. Deslauriers, Non-orbital particle trapping in binary black holes through dynamic stability (2025), arXiv:2503.17841 [astro-ph.HE].
 - [12] R. I. Thompson, T. J. Harmon, and M. G. Ball, The rotating-saddle trap: a mechanical analogy to RF-electric-quadrupole ion trapping?, *Canadian Journal of Physics* **80**, 1433 (2002).
 - [13] O. N. Kirillov and M. Levi, Rotating saddle trap as foucault's pendulum, *American Journal of Physics* **84**, 26 (2016).
 - [14] W. Fan, L. Du, S. Wang, and H. Zhou, Confining rigid balls by mimicking quadrupole ion trapping, *American Journal of Physics* **85**, 821 (2017).
 - [15] A. V. Borisov, A. A. Kilin, and I. S. Mamaev, A nonholonomic model of the paul trap, *Regular and Chaotic Dynamics* **23**, 339 (2018).
 - [16] A.-L. Biance, C. Clanet, and D. Quéré, Leidenfrost drops, *Physics of Fluids* **15**, 1632 (2003).
 - [17] D. Quéré, Leidenfrost dynamics, *Annual Review of Fluid Mechanics* **45**, 197 (2013).
 - [18] L. Deslauriers, P. C. Haljan, P. J. Lee, K.-A. Brickman, B. B. Blinov, M. J. Madsen, and C. Monroe, Zero-point cooling and low heating of trapped $^{111}\text{Cd}^+$ ions, *Physical Review A* **70**, 043408 (2004).
 - [19] C. W. Chou, D. B. Hume, T. Rosenband, and D. J. Wineland, Optical clocks and relativity, *Science* **329**, 1630 (2010).
 - [20] T. D. Ladd, F. Jelezko, R. Laflamme, Y. Nakamura, C. Monroe, and J. L. O'Brien, Quantum computing, *Nature* **464**, 45 (2010).
 - [21] A. Carey, L. Barnett, R. Hart, A. Kales, A. Kurmus, and L. Deslauriers, The asymmetric rotating saddle potential as a mechanical analog to the rf paul trap, arXiv preprint arXiv:2504.04095 (2025).
 - [22] D. J. Wineland, C. Monroe, W. M. Itano, D. Leibfried, B. E. King, and D. M. Meekhof, Experimental issues in coherent quantum-state manipulation of trapped atomic ions, *Journal of Research of the National Institute of Standards and Technology* **103**, 259 (1998).

TABLE I. Materials and approximate costs of demonstration setup.

Item	Name	Vendor and Model	Price (USD)	Comment
1	PETG filament	Prusa Prusament	29.99	Price per kilogram. Dark colors recommended for optimal demonstration visibility.
2	3D-print coating	Smooth-On XTC-3D	33.81	
3	Stepper motor	StepperOnline Nema 17 Bipolar 2A (17HS19-2004S1)	9.62	Available in bulk at a discount
4	Microstep Driver	StepperOnline CNC Stepper Motor Driver	28.99	
5	3/4" wooden board	—	—	Optional for use in saddle mount assembly
6	Self-tapping flat-head 8-32 screws	—	—	To affix the 3D-printed mount to the saddle
7	3D printer	Prusa Original i3 MK3S	From 899	Additional expenses for optional accessories, including textured print sheets

```
[1]: import numpy as np
import stl
from stl import mesh

[2]: """
10.22.2023
Based on script from 10.27.2020
Top layer of points in a grid, (x,y, f(x,y)).
Add a bottom layer with same grid structure.
Make side faces.
Make bottom faces. (just two triangles)

Use this file to make an asymmetric saddle.
Positive curvature: a=0.005*22/21.8 = to make 21 mm height at edge.
Negative curvature b = 0.005*19/21.8 = to make -19 mm height at edge.

This file used to generate 2a.stl. This one is P2a.
Import into Prusa slicer and scale by x1.74 to generate desired geometry.
...

import numpy as np
from stl import mesh

N=101
zbottom = -25
a=0.005*42/21.8;
b=-0.005*30/21.8;
vertices = []

#Create a list of vertices in a square pattern with zero at center.
#creates N*2 vertices from 0 to N*2-1
for i in range(N):
    for j in range(N):
        x=i-(N-1)/2
        y=j-(N-1)/2
        z=a*x**2-b*y**2          #function of x and y.
        vertices.append([x, y, z])

#Add to the list of vertices to make the bottom at z=-1.
#list should have 2N*2 vertices after this.
for i in range(N):
    for j in range(N):
        x=i-(N-1)/2
        y=j-(N-1)/2
        z=zbottom
        vertices.append([x, y, z])

vertices = np.array(vertices)    #turn the list into an array
faces = []

#make faces for top surface. Use grid pattern and cover the area using all vertices.
#
for i in range(N-1):
    for j in range(N-1):
        faces.append([i*N+j, (i+1)*N+j, i*N+j+1])
        faces.append([i*N+j+1, (i+1)*N+j+1, (i+1)*N+j+1])

#make faces for sides.
#
for i in range(N-1):
    faces.append([i*N, N+2*(i+1)*N-1, N+2*(i+1)*N])    #front - neg y faces
    faces.append([i*N, N+2*(i+1)*N, (i+1)*N])

for j in range(N-1):
    faces.append([(N-1)*N+j, N+2*(N-1)*N+j, N+2*(N-1)*N+j+1])    #pos x side.
    faces.append([(N-1)*N+j, N+2*(N-1)*N+j+1, (N-1)*N+j+1])

for j in range(N-1):
    faces.append([j, N+2*j+1, N+2*j+1])    #neg x side.
    faces.append([j, j+1, N+2*j+1])

for i in range(N-1):
    faces.append([(i+1)*N-1, N+2*(i+2)*N-1, N+2*(i+1)*N-1 ])    #front - neg y faces
    faces.append([(i+1)*N-1, (i+2)*N-1, N+2*(i+2)*N-1])

faces.append([29, 29, 45])    #two faces for the bottom
faces.append([45, 29, 49])

faces = np.array(faces)    #turn the list into an array

# Create the mesh
surf = mesh.Mesh(np.zeros(faces.shape[0], dtype=mesh.Mesh.dtype))
for i, f in enumerate(faces):
    for j in range(3):
        surf.vectors[i][j] = vertices[f[j],:]

# Write the mesh to file "plane.stl"
surf.save('2a.stl')

#faces
```

FIG. 9. Python script for generating customizable saddle geometry. Users may vary parameters to achieve different asymmetries and curvatures.

[23] L. Deslauriers, *Cooling and Heating of the Quantum Motion of Trapped Cd Ions*, Ph.d. dissertation, University of Michigan (2007).

[24] K. Miller, N. Lasry, B. Lukoff, J. Schell, and E. Mazur, Use of a scene-based interactive technique to promote active learning in large lecture classes, *Physical Review Special Topics - Physics Education Research* **10**, 020103 (2014).

[25] E. Mazur, *Peer Instruction: A User's Manual* (Prentice Hall, 1997).

[26] OpenAI, ChatGPT-4: Language Model for Dialogue, <https://www.openai.com/> (2023).

[27] S. K. Löfgren *et al.*, Rolling balls or trapping ions? how students relate models to real-world phenomena in the physics laboratory, *Science Education* **107**, 1215 (2023).

[28] S. K. Löfgren, R. M. Fragoso, J. Weidow, and J. Enger, The mechanical paul trap: Introducing the concept of ion trapping, *The Physics Teacher* **61**, 762 (2023).

[29] H. Häffner, C. F. Roos, and R. Blatt, Quantum computing with trapped ions, *Physics Reports* **469**, 155 (2008), arXiv:0809.4368 [quant-ph].

[30] L. Neslušan, On the global electrostatic charge of stars, *Astronomy and Astrophysics* **372**, 913 (2001).

[31] M. Zajaček, A. Tursunov, A. Eckart, and S. Britzen, On the charge of the Galactic centre black hole, *MNRAS* **480**, 4408 (2018), arXiv:1808.07327 [astro-ph.GA].

[32] R. M. Wald, Black hole in a uniform magnetic field, *Physical Review D* **10**, 1680 (1974).

[33] P. Adari, R. Berens, and J. Levin, Charging up boosted black holes, *Physical Review D* **107**, 044055 (2023).

[34] I. J. Araya, N. D. Padilla, M. E. Rubio, J. Sureda, J. Magaña, and L. Osorio, Dark matter from primordial black holes would hold charge, *Journal of Cosmology and Astroparticle Physics* **2023** (2), 030, arXiv:2207.05829 [astro-ph.CO].

[35] C. Kehle and R. Unger, Gravitational collapse to extremal black holes and the third law of black hole thermodynamics, arXiv e-prints, arXiv:2211.15742 (2022), arXiv:2211.15742 [gr-qc].

[36] R. Banerjee and K. Jedamzik, Evolution of cosmic magnetic fields: From the very early Universe, to recombination, to the present, *Phys. Rev. D* **70**, 123003 (2004), arXiv:astro-ph/0410032 [astro-ph].

[37] V. Cardoso, C. F. B. Macedo, P. Pani, and V. Ferrari, Black holes and gravitational waves in models of minicharged dark matter, *Journal of Cosmology and Astroparticle Physics* **2016** (5), 054, arXiv:1604.07845 [hep-ph].

[38] M. Zajacek and A. Tursunov, The Electric Charge of Black Holes: Is It Really Always Negligible, *The Observatory* **139**, 231 (2019), arXiv:1904.04654 [astro-ph.GA].

[39] G. Cox and M. Levi, The ponderomotive lorentz force, *Nonlinearity* **33**, 4030 (2020).

[40] O. N. Kirillov and M. Levi, A coriolis force in an inertial frame, *Nonlinearity* **30**, 1109 (2017).